An Alternating-Direction Hybrid Implicit-Explicit Finite-Difference Time-Domain Method for the Schrödinger Equation.

Pieter Decleer[a,b,*], Arne Van Londersele[b], Hendrik Rogier[b], Dries Vande Ginste[a]

[a] *Quest/IDLab, Department of Information Technology, Ghent University/imec, Technologiepark-Zwijnaarde 126, Ghent, Belgium*

[b] *Electromagnetics Group/IDLab, Department of Information Technology, Ghent University/imec, Technologiepark-Zwijnaarde 126, Ghent, Belgium*

Abstract

This paper proposes a novel hybrid FDTD method for solving the time-dependent Schrödinger equation, which is fundamental for modeling materials and designing nanoscale devices. The wave function is propagated on nonuniform grids by applying explicit updates in part of the grid and implicit updates elsewhere. The latter are based on the Alternating-Direction Implicit (ADI) scheme while the former are constructed with a central difference for the time derivative. A rigorous stability analysis proves that spatial steps can be selectively removed from the stability criterion thus combining the unconditional stability of the ADI scheme with fast explicit calculations. The scheme excels in its flexibility by efficiently discretizing and balancing explicit with implicit updates, as such expediting the computations. Moreover, it retains the linear complexity of explicit schemes with respect to space and time, making it especially scalable to numerically large problems. Several numerical experiments, including a laterally tunnel-coupled quantum wire and a nanowire double-barrier resonant-tunneling diode, show the validity of the scheme by demonstrating its high accuracy and decreased CPU time compared to traditional methods.

Keywords: Finite-difference time-domain (FDTD), Schrödinger equation, Stability, Nonuniform, Alternating-direction hybrid implicit-explicit (ADHIE)

1. Introduction

Downscaling of electronic components has led to the study, design and manufacturing of a variety of new nanoscale devices utilizing, as part of their design, quantum wires [1–7] or quantum waveguides [8–11], which are made from highly promising recently developed materials [12–15]. To understand, model and design these devices, it is imperative to solve the Schrödinger equation with numerical techniques since only a limited number of analytical solutions exist. The study of electron movement far from equilibrium or transient behavior is best tackled by a time-domain method [16, 17], which solves the time-dependent Schrödinger equation. Depending on the structure of interest, one can either solve the effective-mass Schrödinger equation [2, 5, 18] or opt for an ab-initio method, such as Time-Dependent Density Functional Theory (TD-DFT) [19].

The finite-difference time-domain (FDTD) method is frequently applied to solve the Schrödinger equation in the time domain. A multitude of different implementations exist, depending on the spatial discretization and the time propagation, each having their strengths and weaknesses. Moreover, the FDTD method has also been applied to various related equations such as the non-linear Schrödinger equation [20–26], the Gross-Pitaevskii equations [27], and the stationary Schrödinger equation by performing a Wick rotation [28–31].

*Corresponding author

Email address: pieter.decleer@ugent.be (Pieter Decleer)

One of the first time-integration methods applied to the Schrödinger equation, was the Crank-Nicolson (CN) method [32, 33]. Because the method is unitary and stable independent of the time step, it is still widely used to this day [5, 11, 34]. Unconditional stability comes at the cost of implicit time integration for which a system of linear equations has to be solved at every iteration. In 1-D systems, this does not pose a large restriction on its applicability because the linear system is tridiagonal and the number of operations to solve this system scales linearly with its size. However, in 3-D, the system is not solved as easily and will not scale linearly. This makes the CN method excessively slow, particularly for large systems.

Another frequently used implicit method is the alternating-direction implicit (ADI) method [35–37]. It is an adaptation of the CN method that is also unconditionally stable but can instead retain the linear complexity in 2-D and 3-D by solving multiple tridiagonal systems. It is thus better suited for tackling large problems. Based on this method, various implementations exist that deal with the Schrödinger equation [22, 24, 38, 39].

Explicit methods, in which no linear system has to be solved whatsoever, scale linearly with the size of the system and are ideally suited for large systems. In [40], the wave function at a particular point in time is calculated from the wave function at two previous time values. While explicit methods do not involve the solution of a linear system, they are limited by restrictions on the time step. Small spatial steps and high potential energies lead to small time steps. However, it was recently shown that the potential energy surface can be shifted to obtain a larger time step [41]. In [42], the wave function is split in its real and imaginary parts, resulting in a leapfrog scheme. This method was shown in [41] to be mathematically equivalent to the method in [40] but computationally more efficient and it has been extensively discussed [41–44]. The method has been successfully applied to determine the eigenenergies, eigenfunctions and transmission probability through quantum structures [7, 45–47]. Generalizations of this method to higher-order accurate time integrations and to N-particle systems were presented in [48] and [49], respectively.

The above methods are generally formulated on uniform grids, which are composed of identical rectangles or cuboids in 2-D or 3-D, respectively. In some cases, especially for multiscale geometries, it is not necessary to have very small cells everywhere, but only where the potential surface is singular or exhibits a large gradient. In those cases, it is advised to allow the grid to adapt to its environment [41, 50, 51], instead of averaging the potential surface to accommodate the rigid grid [7]. The main advantage of such a nonuniform discretization lies in the drastic reduction of spatial variables, while the main downside is that the time step is still limited by the smallest spatial step. A scheme that allows nonuniform grids and is not hindered by extremely small time steps or expensive calculations, is still unavailable.

In this paper, a new hybrid implicit-explicit (HIE) method for solving the linear time-dependent Schrödinger equation on nonuniform grids is proposed. Whereas HIE methods have already been developed and applied successfully for Maxwell's equations [52–60], similar methods for the Schrödinger equation are still lacking. The main difference between Maxwell's equations and the Schrödinger equation to develop HIE methods is that the Schrödinger equation has a second-order spatial derivative while Maxwell's equations require discretization of the curl operator. Moreover, the Schrödinger equation deals with a complex scalar wave function while Maxwell's equations describe real electric and magnetic vector fields. However, both for Maxwell's equations and the Schrödinger equation, HIE methods tailor the grid to the structure and lower the number of spatial variables in regions of less interest. Implicit updates are applied to regions with small spatial steps and explicit updates to the remainder, resulting in a HIE update scheme. The small spatial steps in the implicitly updated region are removed from the stability criterion, drastically increasing the time step and decreasing the computation time. This makes these techniques ideally suited to tackle highly multiscale geometries. For the novel alternating-direction hybrid implicit-explicit (ADHIE) method for the Schrödinger equation developed in this work, the desirable linear time complexity of an explicit update scheme is retained, making it attractive for large problems and long-time propagation. The flexibility of this scheme enables to optimize the simulation by balancing implicit with explicit updates, consequently increasing both the accuracy and the efficiency compared to traditional schemes.

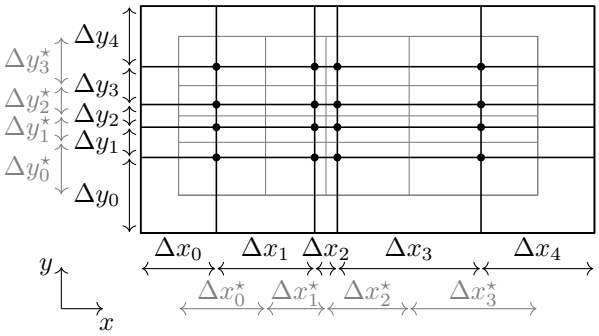

Figure 1: A 2-D slice in the xy-plane of a representative grid with $n_x = n_y = 5$. The primary grid is black and the dual grid is gray. The dual-grid steps are denoted by a star. The $(n_x - 1)(n_y - 1)$ dots represent the discretized wave function, which is defined on the vertices of the primary grid, excluding the edge of the grid.

In the following, Section 2 describes the spatial and temporal discretization resulting in the HIE scheme. Section 3 derives how the scheme eliminates spatial steps from the stability criterion. The accuracy and efficiency of the method is illustrated with several relevant and challenging examples in Section 4. Finally, Section 5 highlights the most important results and presents some challenges expected in future research.

2. Discretization

In this section, we discuss the spatial and temporal discretization of the novel, advocated scheme. In Sections 2.1 and 2.2, we first present the general spatial and temporal discretization scheme for the full 3-D case in matrix notation. This yields the most compact form and facilitates a rigorous stability analysis (see Section 3). Moreover, it leads to a straightforward implementation through sparse matrices and sparse linear algebra solvers included in, e.g., Matlab or Python. However, it offers only limited insight in the actual calculations by the numerical scheme and it is also less used in the FDTD community. Therefore, the numerical scheme for the 2-D case is written in more common expressions in Section 2.3.

2.1. Spatial discretization

The Schrödinger equation is spatially discretized as in [41] on a nonuniform tensor-product grid containing $n_x \times n_y \times n_z$ rectangular cuboids. A slice in the xy-plane of a possible grid is represented in Fig. 1. The spatial discretization of the time-dependent Schrödinger equation on this grid results in

$$\jmath\hbar\frac{\partial}{\partial t}\boldsymbol{\psi} = (T + V)\,\boldsymbol{\psi}, \tag{1}$$

where $\boldsymbol{\psi}$ is the row-major vectorized wave function with length $n = (n_x - 1)(n_y - 1)(n_z - 1)$, $\jmath$ is the imaginary unit and $\hbar$ is the reduced Planck constant $\hbar = 6.582\,119\,6 \times 10^{-16}\,\mathrm{eV\,s}$. The potential matrix $V \in \mathbb{R}^{n\times n}$ is diagonal and contains the values of the potential energy on the vertices of the grid. The discrete kinetic energy operator $T \in \mathbb{R}^{n\times n}$ is defined as

$$T = \frac{\hbar^2}{2m}\left(\left(\delta_x^{\star\,-1} D_x^T \delta_x{}^{-1} D_x\right) \oplus \left(\delta_y^{\star\,-1} D_y^T \delta_y{}^{-1} D_y\right) \oplus \left(\delta_z^{\star\,-1} D_z^T \delta_z{}^{-1} D_z\right)\right) \tag{2}$$

where m is the particle mass, $\oplus$ is the Kronecker sum, $D_u \in \mathbb{R}^{n_u\times(n_u-1)}$ is the discrete differentiator

$$D_u = \begin{bmatrix} -1 & & & \\ 1 & -1 & & \\ & \ddots & \ddots & \\ & & 1 & -1 \\ & & & 1 \end{bmatrix}_{n_u\times(n_u-1)}, \tag{3}$$

and δ_u and $\delta_u^\star$ are diagonal matrices containing the n_u primary and $n_u - 1$ dual grid steps in the u-direction, respectively ($u \in \{x, y, z\}$).

2.2. Temporal discretization

The ADI method [22, 24, 39, 61] is modified and applied *locally* to the explicit update scheme in [41–43, 45, 46]. Unlike existing ADI methods, the wave function $\boldsymbol{\psi}$ is split into its real part $\boldsymbol{r}$ and its imaginary part $\boldsymbol{s}$, which allows to combine explicit and implicit updates. The real and imaginary parts are staggered in time and combined in $\boldsymbol{x}$ as

$$\boldsymbol{x}|^n = \begin{bmatrix} \boldsymbol{r}|^n \\ \boldsymbol{s}|^{n-1/2} \end{bmatrix}, \tag{4}$$

where the superscript denotes the temporal index. The resulting novel ADHIE scheme is

$$\begin{bmatrix} G & -\Delta\nu H \\ 0 & G \end{bmatrix} \boldsymbol{x}|^{n+1} = \begin{bmatrix} G & 0 \\ -\Delta\nu H & G \end{bmatrix} \boldsymbol{x}|^n, \tag{5}$$

where

$$G = \bigotimes_{u\in\{x,y,z\}} \left(I_{n_u-1} + \frac{\Delta\nu}{2} S_u \right), \tag{6}$$

with $\otimes$ denoting the Kronecker product. The discretized Hamiltonian matrix is given by

$$H = T_x \oplus T_y \oplus T_z + V, \tag{7}$$

$\Delta\nu$ is the normalized time step $\Delta\nu = \Delta t/\hbar$. The 1-D kinetic energy operator T_u and the implicitized 1-D kinetic energy operator S_u are defined as

$$T_u = \frac{\hbar^2}{2m} \left(\delta_u^{\star -1} D_u^T \delta_u{}^{-1} D_u \right), \tag{8}$$

$$S_u = \frac{\hbar^2}{2m} \left(\delta_u^{\star -1} D_u^T \delta_u{}^{-1} P_u D_u \right), \tag{9}$$

where $P_u \in \mathbb{R}^{n_u \times n_u}$ is the diagonal projection matrix such that

$$[P_u]_{i,i} = \begin{cases} 0, & \text{if } \Delta u_i \text{ yields an explicit contribution} \\ 1, & \text{if } \Delta u_i \text{ yields an implicit contribution} \end{cases}, \tag{10}$$

and I_n is the $n \times n$ unit matrix. Note that choosing $[P_u]_{i,i} = 0$ for all u and i, produces the fully explicit scheme of [41], whereas $[P_u]_{i,i} = 1$ for all u and i leads to the fully implicit ADI scheme. In the novel ADHIE scheme presented in this paper, $[P_u]_{i,i}$ is carefully chosen to reduce the overall computation time whilst maintaining high accuracy. Similar to the Maxwellian technique [56], our novel Schrödinger technique is also a leapfrog scheme but instead of staggering the electric and magnetic fields in time, the real and imaginary parts of the wave function are staggered. However, where both the real and imaginary parts of the wave function are solved implicitly for the Schrödinger equation, only some components of the electric and magnetic field are solved implicitly for Maxwell's equations. Moreover, although the structure of (5) looks very similar to the update scheme in [56], the occurring matrices are very different. For example, in [56], the curl operator was split whereas here, the structure of the Laplacian operator is exploited.

To maintain the linear time complexity when inverting the matrix in the l.h.s. of (5), it is necessary to exploit the structure of the matrices. This results in a multi-step method, similar to early ADI schemes for Maxwell [54, 62]. However, unlike those schemes, the number of intermediate steps is equal to the number

of implicitized dimensions. The update equations become:

$$\left[\left(I_{n_x-1}+\frac{\Delta\nu}{2}S_x\right)\otimes I_{n_y-1}\otimes I_{n_z-1}\right]\boldsymbol{s}|^{(1)}=-\Delta\nu H\boldsymbol{r}|^{n} \tag{11}$$

$$\left[I_{n_x-1}\otimes\left(I_{n_y-1}+\frac{\Delta\nu}{2}S_y\right)\otimes I_{n_z-1}\right]\boldsymbol{s}|^{(2)}=\boldsymbol{s}|^{(1)} \tag{12}$$

$$\left[I_{n_x-1}\otimes I_{n_y-1}\otimes\left(I_{n_z-1}+\frac{\Delta\nu}{2}S_z\right)\right]\boldsymbol{s}|^{(3)}=\boldsymbol{s}|^{(2)} \tag{13}$$

$$\boldsymbol{s}|^{n+1/2}=\boldsymbol{s}|^{(3)}+\boldsymbol{s}|^{n-1/2} \tag{14}$$

$$\left[\left(I_{n_x-1}+\frac{\Delta\nu}{2}S_x\right)\otimes I_{n_y-1}\otimes I_{n_z-1}\right]\boldsymbol{r}|^{(1)}=\Delta\nu H\boldsymbol{s}|^{n+1/2} \tag{15}$$

$$\left[I_{n_x-1}\otimes\left(I_{n_y-1}+\frac{\Delta\nu}{2}S_y\right)\otimes I_{n_z-1}\right]\boldsymbol{r}|^{(2)}=\boldsymbol{r}|^{(1)} \tag{16}$$

$$\left[I_{n_x-1}\otimes I_{n_y-1}\otimes\left(I_{n_z-1}+\frac{\Delta\nu}{2}S_z\right)\right]\boldsymbol{r}|^{(3)}=\boldsymbol{r}|^{(2)} \tag{17}$$

$$\boldsymbol{r}|^{n+1}=\boldsymbol{r}|^{(3)}+\boldsymbol{r}|^{n} \tag{18}$$

The matrices to be inverted are only nonzero on three of their diagonals and can, hence, be solved by the tridiagonal matrix algorithm of order $\mathcal{O}(n)$ [63]. Even though the separation into real and imaginary parts increases the number of update equations compared to the fully implicit Schrödinger method [24], our novel ADHIE method does not require more storage or more floating-point operations, as no complex arithmetic is required.

2.3. 2-D update equations in scalar notation

To elucidate the inner workings of the method, the 2-D case is now treated, adopting a more common notation for FDTD. In the following update equations (19)–(24), the lower indices represent the spatial indices, as explained in Fig. 1. The 2-D equivalent of (11)–(14) becomes in scalar notation:

$$\begin{aligned}&s|_{i,j}^{(1)}-\frac{\hbar\Delta t}{4m}\left(p_x|_{i+1}\frac{s|_{i+1,j}^{(1)}-s|_{i,j}^{(1)}}{\Delta x_{i+1}\Delta x_i^\star}-p_x|_i\frac{s|_{i,j}^{(1)}-s|_{i-1,j}^{(1)}}{\Delta x_i^\star\Delta x_i}\right)\\&\quad=\frac{\hbar\Delta t}{2m}\left(\frac{r|_{i+1,j}^{n}-r|_{i,j}^{n}}{\Delta x_{i+1}\Delta x_i^\star}-\frac{r|_{i,j}^{n}-r|_{i-1,j}^{n}}{\Delta x_i^\star\Delta x_i}+\frac{r|_{i,j+1}^{n}-r|_{i,j}^{n}}{\Delta y_{j+1}\Delta y_j^\star}-\frac{r|_{i,j}^{n}-r|_{i,j-1}^{n}}{\Delta y_j^\star\Delta y_j}\right)-\frac{\Delta t}{\hbar}V|_{i,j}r|_{i,j}^{n},\end{aligned} \tag{19}$$

$$s|_{i,j}^{(2)}-\frac{\hbar\Delta t}{4m}\left(p_y|_{j+1}\frac{s|_{i,j+1}^{(2)}-s|_{i,j}^{(2)}}{\Delta y_{j+1}\Delta y_j^\star}-p_y|_j\frac{s|_{i,j}^{(2)}-s|_{i,j-1}^{(2)}}{\Delta y_j^\star\Delta y_j}\right)=s|_{i,j}^{(1)}, \tag{20}$$

$$s|_{i,j}^{n+\frac{1}{2}}=s|_{i,j}^{(2)}+s|_{i,j}^{n-\frac{1}{2}}. \tag{21}$$

For (15)–(18) we get:

$$r|_{i,j}^{(1)} - \frac{\hbar\Delta t}{4m}\left(p_x|_{i+1}\frac{r|_{i+1,j}^{(1)} - r|_{i,j}^{(1)}}{\Delta x_{i+1}\Delta x_i^\star} - p_x|_i\frac{r|_{i,j}^{(1)} - r|_{i-1,j}^{(1)}}{\Delta x_i^\star\Delta x_i}\right)$$
$$= -\frac{\hbar\Delta t}{2m}\left(\frac{s|_{i+1,j}^{n+\frac{1}{2}} - s|_{i,j}^{n+\frac{1}{2}}}{\Delta x_{i+1}\Delta x_i^\star} - \frac{s|_{i,j}^{n+\frac{1}{2}} - s|_{i-1,j}^{n+\frac{1}{2}}}{\Delta x_i^\star\Delta x_i} + \frac{s|_{i,j+1}^{n+\frac{1}{2}} - s|_{i,j}^{n+\frac{1}{2}}}{\Delta y_{j+1}\Delta y_j^\star} - \frac{s|_{i,j}^{n+\frac{1}{2}} - s|_{i,j-1}^{n+\frac{1}{2}}}{\Delta y_j^\star\Delta y_j}\right) + \frac{\Delta t}{\hbar}V|_{i,j}s|_{i,j}^{n+\frac{1}{2}}, \tag{22}$$

$$r|_{i,j}^{(2)} - \frac{\hbar\Delta t}{4m}\left(p_y|_{j+1}\frac{r|_{i,j+1}^{(2)} - r|_{i,j}^{(2)}}{\Delta y_{j+1}\Delta y_j^\star} - p_y|_j\frac{r|_{i,j}^{(2)} - r|_{i,j-1}^{(2)}}{\Delta y_j^\star\Delta y_j}\right) = r|_{i,j}^{(1)}, \tag{23}$$

$$r|_{i,j}^{n+1} = r|_{i,j}^{(2)} + r|_{i,j}^{n}. \tag{24}$$

The approximated second-order partial derivative in (19) and (22) is derived in Appendix A. The numerical scheme sequentially solves equations (19)–(24) for all i and j. The scalar $p_u|_i$ represents the i-th diagonal element of the matrix P_u, $u \in \{x, y\}$, and can only assume the value 0 or 1. In this form, it is easily seen that if, e.g., $p_x|_i = p_x|_{i+1} = 0$ for a certain i, (19) and (22) are solved explicitly. In contrast, if $p_x|_i = 1$ for a certain i, (19) is solved implicitly because the value of $s|_{i,j}^{(1)}$ depends on the unknown value $s|_{i-1,j}^{(1)}$ and vice versa. The same reasoning applies to $r|_{i,j}^{(1)}$ and $r|_{i-1,j}^{(1)}$ in (22). Moreover, as will be shown in Section 3, the spatial step Δx_i is removed from the stability criterion by virtue of this local implicitization. Lastly, (19)–(24) clearly illustrate that the implicitization requires at most the solution of a tridiagonal system, even in higher dimensions, which can be done efficiently with the tridiagonal matrix algorithm [64].

3. Stability

In this section, the time step for which the ADHIE scheme is stable is derived. The resulting formula enables the user to tune the time step by selectively removing small spatial steps.

First, the update equations are symmetrized using the diagonal transformation matrix $Q \in \mathbb{R}^{n\times n}$

$$Q \triangleq \delta_x^\star \otimes \delta_y^\star \otimes \delta_z^\star. \tag{25}$$

Left multiplication of (5) with $I_2 \otimes Q^{1/2}$ results in

$$\begin{aligned}&\begin{bmatrix}Q^{1/2} & \\ & Q^{1/2}\end{bmatrix}\begin{bmatrix}G & -\Delta\nu H\\ 0 & G\end{bmatrix}\begin{bmatrix}Q^{-1/2} & \\ & Q^{-1/2}\end{bmatrix}\begin{bmatrix}Q^{1/2} & \\ & Q^{1/2}\end{bmatrix}\boldsymbol{x}|^{n+1}\\ &= \begin{bmatrix}Q^{1/2} & \\ & Q^{1/2}\end{bmatrix}\begin{bmatrix}G & 0\\ -\Delta\nu H & G\end{bmatrix}\begin{bmatrix}Q^{-1/2} & \\ & Q^{-1/2}\end{bmatrix}\begin{bmatrix}Q^{1/2} & \\ & Q^{1/2}\end{bmatrix}\boldsymbol{x}|^{n}.\end{aligned} \tag{26}$$

This simplifies to the symmetrized update equation

$$\begin{bmatrix}\tilde{G} & -\Delta\nu\tilde{H}\\ 0 & \tilde{G}\end{bmatrix}\tilde{\boldsymbol{x}}|^{n+1} = \begin{bmatrix}\tilde{G} & 0\\ -\Delta\nu\tilde{H} & \tilde{G}\end{bmatrix}\tilde{\boldsymbol{x}}|^{n}, \tag{27}$$

with

$$\tilde{\boldsymbol{x}}|^n = \begin{bmatrix}Q^{1/2}\boldsymbol{r}|^n\\ Q^{1/2}\boldsymbol{s}|^{n-1/2}\end{bmatrix}, \tag{28}$$

$$\tilde{H} = \tilde{T}_x \oplus \tilde{T}_y \oplus \tilde{T}_z + V, \tag{29}$$

$$\tilde{G} = \bigotimes_{u\in\{x,y,z\}}\left(I_{n_u-1} + \frac{\Delta\nu}{2}\tilde{S}_u\right), \tag{30}$$

$$\tilde{T}_u = \frac{\hbar^2}{2m}\Big(\delta_u^{\star\,-1/2} D_u^T \delta_u{}^{-1} D_u \delta_u^{\star\,-1/2}\Big), \tag{31}$$

and

$$\tilde{S}_u = \frac{\hbar^2}{2m}\Big(\delta_u^{\star\,-1/2} D_u^T \delta_u{}^{-1} P_u D_u \delta_u^{\star\,-1/2}\Big), \tag{32}$$

where we have used the mixed-product property for the Kronecker product [65]. It is clear that all matrices indicated with a tilde are real and symmetric. Proving the stability of (5) is equivalent to proving the stability of (27).

Following the approach in [56, 66], the symmetrized update scheme (27) is rewritten as

$$(E+F)\tilde{\boldsymbol{x}}|^{n+1} = (E-F)\tilde{\boldsymbol{x}}|^{n}, \tag{33}$$

with

$$E = \begin{bmatrix} \tilde{G} & -\frac{\Delta\nu}{2}\tilde{H} \\ -\frac{\Delta\nu}{2}\tilde{H} & \tilde{G} \end{bmatrix}, \tag{34}$$

and

$$F = \begin{bmatrix} 0 & -\frac{\Delta\nu}{2}\tilde{H} \\ \frac{\Delta\nu}{2}\tilde{H} & 0 \end{bmatrix} \tag{35}$$

Since E is real symmetric and F is real, it is possible to use the results in [66], stating that the scheme is stable if E is positive definite and $F + F^T$ is positive semi-definite. The latter condition is trivially satisfied because $F + F^T$ is the zero matrix. The former is satisfied if the time step satisfies

$$\Delta t < \frac{2\hbar}{\left\| \tilde{U}_x \oplus \tilde{U}_y \oplus \tilde{U}_z + V \right\|_2}, \tag{36}$$

where the matrix $\tilde{U}_u$ is defined as

$$\tilde{U}_u = \frac{\hbar^2}{2m}\Big(\delta_u^{\star\,-1/2} D_u^T (I_{n_u} - P_u) \delta_u{}^{-1} D_u \delta_u^{\star\,-1/2}\Big) \tag{37}$$

$$= \tilde{T}_u - \tilde{S}_u. \tag{38}$$

and $\|\cdot\|_2$ denotes the matrix 2-norm. This is proved by expanding E in six parts $E = \sum_{i=1}^{6} E_i$. Because the Kronecker product is distributive over the matrix sum, $\tilde{G}$ can be expanded as

$$\begin{aligned} \tilde{G} = I_n &+ \frac{\Delta\nu}{2}\Big(\tilde{S}_x \otimes I_{n_y-1} \otimes I_{n_z-1} + I_{n_x-1} \otimes \tilde{S}_y \otimes I_{n_z-1} + I_{n_x-1} \otimes I_{n_y-1} \otimes \tilde{S}_z\Big) \\ &+ \left(\frac{\Delta\nu}{2}\right)^2 \Big(\tilde{S}_x \otimes \tilde{S}_y \otimes I_{n_z-1} + \tilde{S}_x \otimes I_{n_y-1} \otimes \tilde{S}_z + I_{n_x-1} \otimes \tilde{S}_y \otimes \tilde{S}_z\Big) \\ &+ \left(\frac{\Delta\nu}{2}\right)^3 \Big(I_2 \otimes \tilde{S}_x \otimes \tilde{S}_y \otimes \tilde{S}_z\Big). \end{aligned} \tag{39}$$

By also considering that

$$\tilde{T}_x \oplus \tilde{T}_y \oplus T_z = \tilde{U}_x \oplus \tilde{U}_y \oplus \tilde{U}_z + \tilde{S}_x \oplus \tilde{S}_y \oplus \tilde{S}_z, \tag{40}$$

it is easy to obtain the six expansion terms

$$E_1 = \begin{bmatrix} I_n & -\frac{\Delta\nu}{2}\Big(\tilde{U}_x \oplus \tilde{U}_y \oplus \tilde{U}_z + V\Big) \\ -\frac{\Delta\nu}{2}\Big(\tilde{U}_x \oplus \tilde{U}_y \oplus \tilde{U}_z + V\Big) & I_n \end{bmatrix}, \tag{41}$$

$$E_2 = \left(\frac{\Delta\nu}{2}\right)\left(\begin{bmatrix} 1 & -1 \\ -1 & 1 \end{bmatrix} \otimes \Big(\tilde{S}_x \oplus \tilde{S}_y \oplus \tilde{S}_z\Big)\right), \tag{42}$$

$$E_3 = \left(\frac{\Delta\nu}{2}\right)^2 \Big(I_2 \otimes \tilde{S}_x \otimes \tilde{S}_y \otimes I_{n_z-1}\Big), \tag{43}$$

$$E_4 = \left(\frac{\Delta\nu}{2}\right)^2 \Big(I_2 \otimes \tilde{S}_x \otimes I_{n_y-1} \otimes \tilde{S}_z\Big), \tag{44}$$

$$E_5 = \left(\frac{\Delta\nu}{2}\right)^2 \Big(I_2 \otimes I_{n_x-1} \otimes \tilde{S}_y \otimes \tilde{S}_z\Big), \tag{45}$$

$$E_6 = \left(\frac{\Delta\nu}{2}\right)^3 \Big(I_2 \otimes \tilde{S}_x \otimes \tilde{S}_y \otimes \tilde{S}_z\Big). \tag{46}$$

Matrices E_2 to E_6 are all positive semi-definite because

$$\sigma(A \oplus B) = \{a + b : a \in \sigma(A) \quad \text{and} \quad b \in \sigma(B)\}, \tag{47}$$

$$\sigma(A \otimes B) = \{ab : a \in \sigma(A) \quad \text{and} \quad b \in \sigma(B)\}, \tag{48}$$

and

$$\sigma\left(\begin{bmatrix} 1 & -1 \\ -1 & 1 \end{bmatrix}\right) = \{0, 2\}, \tag{49}$$

where $\sigma(\cdot)$ denotes the spectrum, and also considering that $\tilde{S}_u$ is positive semi-definite since

$$\begin{aligned} \boldsymbol{x}^T \tilde{S}_u \boldsymbol{x} &= \frac{\hbar^2}{2m} \boldsymbol{x}^T \Big({\delta_u^\star}^{-1/2} D_u^T P_u {\delta_u}^{-1} P_u D_u {\delta_u^\star}^{-1/2}\Big)\boldsymbol{x} \\ &= \frac{\hbar^2}{2m} \Big({\delta_u}^{-1/2} P_u D_u {\delta_u^\star}^{-1/2} \boldsymbol{x}\Big)^T {\delta_u}^{-1/2} P_u D_u {\delta_u^\star}^{-1/2} \boldsymbol{x} \\ &= \frac{\hbar^2}{2m} \Big\| {\delta_u}^{-1/2} P_u D_u {\delta_u^\star}^{-1/2} \boldsymbol{x} \Big\|_2^2 \geq 0 \quad \forall \boldsymbol{x} \in \mathbb{R}^n. \end{aligned} \tag{50}$$

Matrix E_1 is positive definite if and only if

$$\boldsymbol{x}^T E_1 \boldsymbol{x} = \|\boldsymbol{x}\|_2^2 - \boldsymbol{x}^T \hat{E}_1 \boldsymbol{x} > 0 \quad \forall \boldsymbol{x} \in \mathbb{R}^{2n} \setminus \boldsymbol{0}, \tag{51}$$

where $\hat{E}_1$ is defined as

$$\hat{E}_1 = \frac{\Delta\nu}{2} \begin{bmatrix} 0 & 1 \\ 1 & 0 \end{bmatrix} \otimes \Big(\tilde{U}_x \oplus \tilde{U}_y \oplus \tilde{U}_z + V\Big). \tag{52}$$

This is equivalent to

$$\max_{\boldsymbol{x} \in \mathbb{R}^{2n} \setminus \boldsymbol{0}} \frac{\boldsymbol{x}^T \hat{E}_1 \boldsymbol{x}}{\|\boldsymbol{x}\|_2^2} = \lambda_{\max}(\hat{E}_1) < 1, \tag{53}$$

where we have used [65, eq. 8.4.3]. The maximum eigenvalue of $\hat{E}_1$ is equal to

$$\lambda_{\max}(\hat{E}_1) = \frac{\Delta\nu}{2} \rho(\tilde{U}_x \oplus \tilde{U}_y \oplus \tilde{U}_z + V), \tag{54}$$

where $\rho(\cdot)$ is the spectral radius. The transition from $\lambda_{\max}$ to spectral radius, is important since the matrix $\tilde{U}_x \oplus \tilde{U}_y \oplus \tilde{U}_z + V$ is not necessarily positive definite. Given that the spectral radius of a symmetric matrix

is equal to the 2-norm of the matrix [64, Cor. 1.8], the combination of (53) and (54) yields (36), which concludes the proof. Moreover, as the spectral radius is bounded by any induced norm – such as the 1- or infinity norm – it is also possible to use these norms to get an estimate for the time step. This leads to a Courant-like stability condition, known from FDTD algorithms for Maxwell's equations with, however, several important differences such as the presence of a background potential and the scaling of the time step with the square of the smallest spatial steps, as already shown in [41]. This squared scaling relation highlights the need for a Schrödinger HIE scheme that can eliminate the small steps from the stability criterion.

To clearly see the difference between the fully explicit and the hybrid implicit-explicit scheme, it is instructive to derive a Courant-like stability criterion just as in [41] for the fully explicit scheme. We will only consider the 2-D case for ease of notation. The 2-D stability criterion – approximately calculated with the infinity norm – is:

$$\Delta t < \frac{2\hbar}{\|U_x \oplus U_y + V\|_\infty} \tag{55}$$

$$= \frac{2\hbar}{\max\limits_k \left(\sum\limits_l |[U_x \oplus U_y + V]_{k,l}| \right)}, \quad \text{for} \quad k,l \in \{0,\ldots,(n_x-1)(n_y-1)\} \tag{56}$$

$$= \frac{2\hbar}{\max\limits_{i,j} \left(\frac{\hbar^2}{2m} \left(\frac{1}{\Lambda_{i,j}} \right)^2 + \left| \frac{\hbar^2}{2m} \left(\frac{1}{\Lambda_{i,j}} \right)^2 + V|_{i,j} \right| \right)} \tag{57}$$

with

$$\left(\frac{1}{\Lambda_{i,j}} \right)^2 = \frac{1-p_x|_i}{\Delta x_i \Delta x_i^\star} + \frac{1-p_x|_{i+1}}{\Delta x_{i+1} \Delta x_i^\star} + \frac{1-p_y|_j}{\Delta y_j \Delta y_j^\star} + \frac{1-p_y|_{j+1}}{\Delta y_{j+1} \Delta y_j^\star}. \tag{58}$$

By assuming $V|_{i,j} > -\hbar^2/(2m{\Lambda_{i,j}}^2)$, we can simplify (57) as:

$$\Delta t < \frac{2\hbar}{\max\limits_{i,j} \left(\frac{\hbar^2}{m} \left(\frac{1}{\Lambda_{i,j}} \right)^2 + V|_{i,j} \right)}. \tag{59}$$

In contrast, the time step for the fully explicit method has to satisfy:

$$\Delta t < \frac{2\hbar}{\max\limits_{i,j} \left(\frac{\hbar^2}{m} \left(\frac{1}{K_{i,j}} \right)^2 + V|_{i,j} \right)} \tag{60}$$

with

$$\left(\frac{1}{K_{i,j}} \right)^2 = \frac{1}{\Delta x_i \Delta x_i^\star} + \frac{1}{\Delta x_{i+1} \Delta x_i^\star} + \frac{1}{\Delta y_j \Delta y_j^\star} + \frac{1}{\Delta y_{j+1} \Delta y_j^\star} \tag{61}$$

This clearly shows that the hybrid scheme can remove specific Δx_i or Δy_j from the stability criterion by setting $p_x|_i = 1$ and $p_y|_j = 1$, respectively. Moreover, because (61) is always greater than or equal to (58), the stability criterion for the ADHIE scheme (59) is *less* restrictive. Consequently, the hybrid scheme can support much higher time steps, granted that the smallest cells are removed from the stability criterion.

4. Examples

In this section, first, two possibilities for a hybrid implicit-explicit scheme are theoretically discussed to explain the inner workings of the method in greater detail. Secondly, the method is demonstrated numerically via application to two relevant examples.

Δx	2.0 nm	1.0 nm	0.5 nm	0.25 nm
Δt	17.276 fs	4.3190 fs	1.0797 fs	0.269 94 fs

Table 1: The time steps for the successively refined grids in Section 4.3 are calculated with (57).

4.1. Implicitization of a single direction

Consider a grid that is discretized very densely in a single direction, e.g., the x-direction. By choosing $P_x = I_{n_x}$, matrix $\tilde{U}_x$ is reduced to the zero matrix. Consequently, the time step must satisfy

$$\Delta t < \frac{2\hbar}{\left\| I_{n_x-1} \otimes \left(\tilde{T}_y \oplus \tilde{T}_z \right) + V \right\|_2}. \tag{62}$$

The matrix $I_{n_x-1} \otimes \left(\tilde{T}_y \oplus \tilde{T}_z \right) + V$ is block diagonal where each block corresponds to a slice in the yz-plane. Consequently, it is easy to see that the time step must satisfy a 2-D stability condition for every slice. Moreover, solving a single direction implicitly significantly simplifies the update equations compared to the traditional multistep 3-D ADI schemes mentioned above, since we can now iterate in a leapfrog manner. Indeed, starting from (5) with $P_x = I_{n_x}$, $P_y = 0$ and $P_z = 0$ (i.e., the x-direction is fully implicitized and the updates in the yz-plane are fully explicit), we get:

$$\left[\left(I_{n_x-1} + \frac{\Delta\nu}{2} T_x \right) \otimes I_{n_y-1} \otimes I_{n_z-1} \right] \boldsymbol{s}|^{n+1/2} = \left[\left(I_{n_x-1} + \frac{\Delta\nu}{2} T_x \right) \otimes I_{n_y-1} \otimes I_{n_z-1} \right] \boldsymbol{s}|^{n-1/2} - \Delta\nu H \boldsymbol{r}|^n, \tag{63}$$

and

$$\left[\left(I_{n_x-1} + \frac{\Delta\nu}{2} T_x \right) \otimes I_{n_y-1} \otimes I_{n_z-1} \right] \boldsymbol{r}|^{n+1} = \left[\left(I_{n_x-1} + \frac{\Delta\nu}{2} T_x \right) \otimes I_{n_y-1} \otimes I_{n_z-1} \right] \boldsymbol{r}|^n + \Delta\nu H \boldsymbol{s}|^{n+1/2}. \tag{64}$$

4.2. Local 1-D implicitization

When the discretization is chosen nonuniform along a single direction (chosen to be the x-direction, as in the previous subsection), it is unnecessary to completely solve this direction implicitly. Such local grid refinement can be used to resolve small geometric details. The update scheme for this local implicitization, and leaving the yz-plane fully explicit, is again the leapfrog scheme (63) and (64) with T_x replaced by S_x. This renders the matrix on the left-hand sides sparser still.

4.3. Convergence of solution at implicit-explicit interface

In this section, we will study the convergence order of the hybrid FDTD scheme. Therefore a 2-D free wave packet with mass $m = m_\mathrm{e} = 9.109\,383\,701\,5 \times 10^{-31}$ kg is simulated traveling diagonally along $x = y$, on a uniform grid of 1100 nm × 1100 nm. The convergence of the hybrid implicit-explicit scheme is studied by successively refining the grid with spatial steps $\Delta x = \Delta y \in \{2.0\,\mathrm{nm}, 1.0\,\mathrm{nm}, 0.5\,\mathrm{nm}, 0.25\,\mathrm{nm}\}$. The wave function is updated fully explicitly from $x = 0.0$ nm to $x = 500.0$ nm. In the other part of the grid, i.e., from $x = 500.0$ nm to $x = 1100.0$ nm, the wave function is updated with implicitization in the x-direction. The simulation set-up is sketched in Fig. 2. The time step is calculated with the Courant-like stability criterion (57). Because the grid is uniform, local implicitization does not affect the time step. As such, only the accuracy is studied. The efficiency is sufficiently tested in Sections 4.4 and 4.5. The resulting time steps are given in Table 1. The initial wave function is given by:

$$\psi(x,y) = \frac{\pi}{\sigma^2} e^{-\jmath \frac{\sqrt{2mE_c}}{\hbar}((x-x_0)+(y-y_0))} e^{-\frac{1}{4}\frac{(x-x_0)^2+(y-y_0)^2}{\sigma^2}}, \tag{65}$$

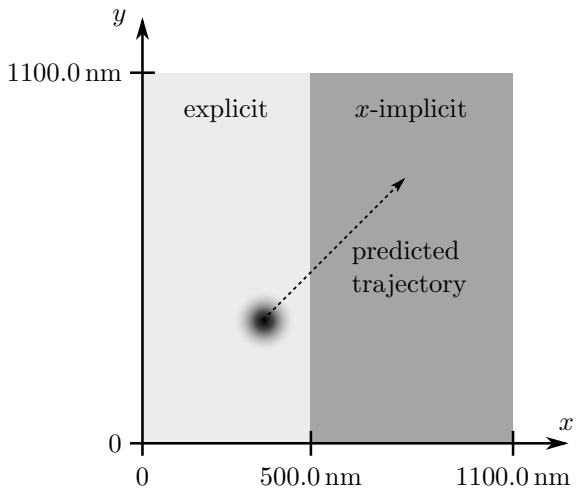

Figure 2: The square grid of 1100.0 nm × 1100.0 nm is split into a part that is updated fully explicit and a part that is updated with implicitization in the x-direction. The interface between these two regions is positioned at $x = 500.0\,\mathrm{nm}$. A free Gaussian wave packet is initialized at $x = y = 300.0\,\mathrm{nm}$ and it travels along the diagonal $x = y$ in the direction of the implicitized part of the grid.

with

$$E_c = 0.02\,\mathrm{eV}, \tag{66}$$
$$\sigma = 30.0\,\mathrm{nm}, \tag{67}$$
$$x_0 = y_0 = 300.0\,\mathrm{nm}. \tag{68}$$

To quantify the convergence of the ADHIE scheme, the expectation value of the position is tracked as a function of time and compared to the analytic result. The time-averaged error is given by:

$$\mathcal{E} = \sqrt{\frac{1}{T}\int_0^T \left\| \langle \hat{\boldsymbol{r}}_{\mathrm{calc}}(t) \rangle - \langle \hat{\boldsymbol{r}}_{\mathrm{ana}}(t) \rangle \right\|^2 \mathrm{d}t}, \tag{69}$$

where $T = 6000\,\mathrm{fs}$ is the total simulation time, $\langle \hat{\boldsymbol{r}}_{\mathrm{ana}}(t) \rangle$ is the analytical position and $\langle \hat{\boldsymbol{r}}_{\mathrm{calc}}(t) \rangle$ is the calculated position. At the interface $x = 500.0\,\mathrm{nm}$ of the explicit and HIE parts of the grid, artificial reflection of the wave function might appear. To quantify this spurious reflection, the probability of finding the particle in the area $0\,\mathrm{nm} < x < 500\,\mathrm{nm}$ is calculated at time $t = 5000\,\mathrm{fs}$. At that time the analytical wave packet in front of the barrier ($x < 500\,\mathrm{nm}$) is negligible and the particle has passed the interface at $x = 500\,\mathrm{nm}$ completely. Hence, the reflection coefficient R is calculated as:

$$R = \int_{0\,\mathrm{nm}}^{500\,\mathrm{nm}} \mathrm{d}x \int_{0\,\mathrm{nm}}^{1100\,\mathrm{nm}} \mathrm{d}y \, |\psi(x,y)|^2. \tag{70}$$

The errors $\mathcal{E}$ and reflection coefficients R for the varying cell sizes are given in Figs. 3a and 3b, respectively. For this example, the error $\mathcal{E}$ converges approximately as $\mathcal{O}\left(\Delta x^{2.85}\right)$ and the reflection probability R decreases as $\mathcal{O}\left(\Delta x^{5.06}\right)$. This shows that the ADHIE method scales very well with decreasing cell sizes.

4.4. Flying qubit in laterally tunnel-coupled quantum wires

In this section, a flying qubit interferometer is simulated in the time domain. These kinds of devices have been numerically investigated in [67–70] and also fabricated in, e.g., [71]. The active region is constructed on the interface of a GaAs/AlGaAs heterostructure, creating a 2-D electron gas. The device itself is shown

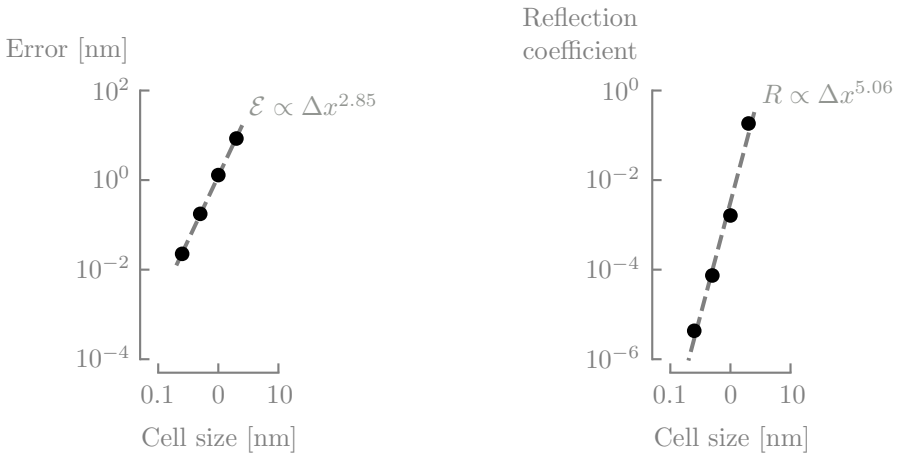

(a) Error convergence

(b) Reflection probability

Figure 3: The time-averaged error $\mathcal{E}$ and spurious reflection coefficient R scale very well with the cell sizes. For the tested cell sizes of $\Delta x = 2.0\,\text{nm}$, $1.0\,\text{nm}$, $0.5\,\text{nm}$ and $0.25\,\text{nm}$, the error $\mathcal{E}$ converges as $\mathcal{O}\big(\Delta x^{2.85}\big)$ and the reflection probability R decreases as $\mathcal{O}\big(\Delta x^{5.06}\big)$.

in Fig. 4 and consists of two parallel quantum wires separated by a thin and high barrier, and a central scattering region of length w where the barrier height is variable. An electron in the upper or lower channel is denoted by $|\uparrow\rangle$ or $|\downarrow\rangle$, respectively. In the central region, it is possible for an electron originally in state $|\downarrow\rangle$ to tunnel from the lower channel to the upper channel $|\uparrow\rangle$. The final state of the electron will be a superposition of the $|\uparrow\rangle$ and $|\downarrow\rangle$ state, depending on the length w of the interaction region, and the – potentially time-dependent – barrier height.

The device geometry studied here is very similar to the geometry presented in [69]. The entire length of the device is $L = 1970\,\text{nm}$. The widths of the channels are $d_1 = d_2 = 28\,\text{nm}$ and the width of the barrier is $h = 2\,\text{nm}$. The spatial step in the x-direction is $\Delta x = 1\,\text{nm}$. Both channels are uniformly discretized in the y-direction with $\Delta y_{\text{ch}} = 1\,\text{nm}$ and the barrier is uniformly discretized with $\Delta y_{\text{bar}} = 0.2\,\text{nm}$. Along the length of the channel, the simulation domain is truncated by a $50\,\text{nm}$ thick PML [23, 41, 47] to simulate an unbounded domain and the channels are terminated by Dirichlet boundary conditions in the y-direction. Hence, the resulting grid contains 1970×66 cells. The potential for the barrier outside of the central region is set to $V = 0.5\,\text{eV}$ whereas the potential in the central region V_b is variable. The effective mass of the wave packet is set to $m = 0.067\,m_{\text{e}}$. The first set of calculations considers a central region with a static barrier. The second set of calculations considers a time-dependent barrier.

A static barrier of length $l = 250\,\text{nm}$ is chosen in the central region, starting $500\,\text{nm}$ from the left side. Simulations are performed for different barrier heights and using the different time integration techniques: explicit, ADHIE and CN. For the ADHIE method, only the small cells in the y-direction are implicitly solved, similar to what was proposed in Section 4.2. The results are also compared to the explicit scheme using a coarse uniform discretization – as opposed to the fine discretization presented above – of $\Delta x = \Delta y = 1\,\text{nm}$ throughout the grid, thus not resolving the barrier accurately. The time steps for the different calculations are as follows:

$$\Delta t_{\text{exp,coarse}} = 270.0\,\text{as}, \qquad \Delta t_{\text{exp,fine}} = 22.65\,\text{as}, \tag{71}$$

$$\Delta t_{\text{ADHIE}} = 289.4\,\text{as}, \qquad \Delta t_{\text{CN}} = 700.0\,\text{as}. \tag{72}$$

Two things are interesting to note here. First, $\Delta t_{\text{exp,coarse}}$ is larger than the time step obtained using the traditional Courant limit in [44], i.e., $\Delta t = 260.4\,\text{as}$. The reason for this is discussed in [41] and can also

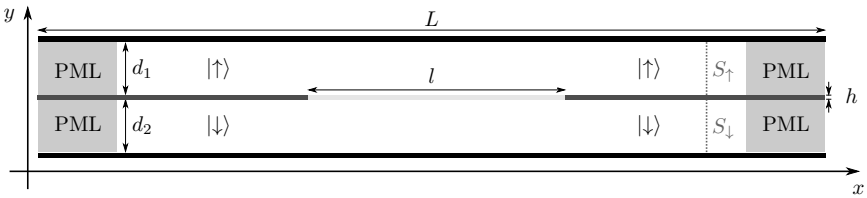

Figure 4: Geometry of the flying qubit interferometer. The width of the upper and lower channel is denoted by d_1 and d_2, respectively. These 2-D channels are separated by a barrier with thickness h. A central scattering region of length l has a variable barrier height V_b and allows interaction between both channels. The channels are terminated on both sides by a PML. An electron originally in the lower channel (state $|\downarrow\rangle$) will leave the channel in a superposition of $|\uparrow\rangle$ and $|\downarrow\rangle$ being both in the upper and lower channels with a given probability. The surfaces $S_\uparrow$ and $S_\downarrow$,indicated with the dotted line, denote the planes through which the probability density current is calculated.

be derived from the stability criterion (36) in the limit of no implicitization. Second, despite using smaller cells with the ADHIE method, the time step $\Delta t_{\mathrm{ADHIE}}$ is larger than $\Delta t_{\mathrm{exp,coarse}}$. This is a consequence of the well-chosen implicitization.
The initial wave packet is entirely confined in the lower channel $|\downarrow\rangle$ and defined by

$$\psi(x,y) = \begin{cases} \sqrt{\frac{2}{d_1}}\cos\left(\frac{\pi y}{d_1}\right)\sqrt{\frac{\pi}{\sigma^2}}e^{-\jmath\frac{\sqrt{2mE_c}}{\hbar}(x-x_0)}e^{-\left(\frac{x-x_0}{2\sigma}\right)^2}, & 0.0\,\mathrm{nm} < y < 29.0\,\mathrm{nm}, \\ 0, & \text{otherwise}, \end{cases} \tag{73}$$

with

$$m = 0.067\,m_{\mathrm{e}}, \tag{74}$$
$$E_c = 0.2\,\mathrm{eV}, \tag{75}$$
$$\sigma = 30.0\,\mathrm{nm}, \tag{76}$$
$$x_0 = 200.0\,\mathrm{nm}. \tag{77}$$

The x-dependence of the wave function represents a Gaussian wave packet traveling in the positive x-direction and the y-dependence is the ground state wave function of a particle-in-a-box of width d_1. In Fig. 5, the probability of finding the electron in the upper or lower channel as a function of the barrier height is shown. These probabilities are derived as

$$N_{\uparrow(\downarrow)} = \frac{1}{N_0}\int_0^{t_{\max}}\int_{S_{\uparrow(\downarrow)}} \boldsymbol{j}\cdot\boldsymbol{n}\,\mathrm{d}S\,\mathrm{d}t\,, \tag{78}$$

with $\boldsymbol{n}$ a normal unit vector to a surface $S_{\uparrow(\downarrow)}$ in the upper (or lower) channel, N_0 the total particle number and $\boldsymbol{j}$ the probability current density

$$\boldsymbol{j} = \frac{\hbar}{m}\,\mathrm{Im}\{\psi^*\boldsymbol{\nabla}\psi\}. \tag{79}$$

As such, the total charge that passed through that channel during the simulation is calculated instead of the instantaneous charge at an arbitrary point in time. The plane at which (78) was evaluated was $x = 1200\,\mathrm{nm}$.

It can be seen that all the simulations except the one using the coarse grid, have matching results. The main difference between the simulations is their calculation time. The computation times for the different

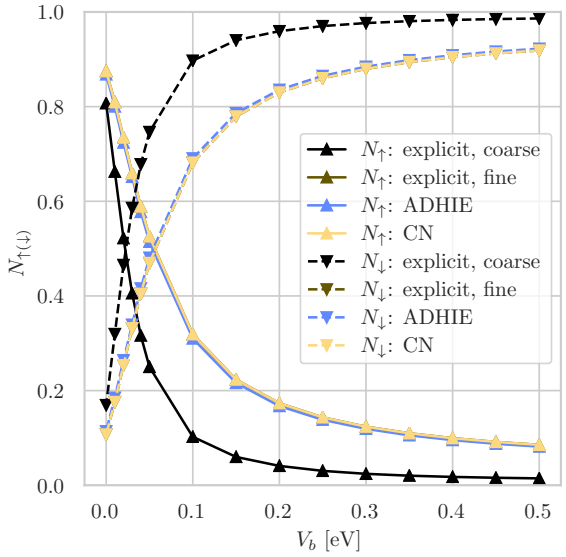

Figure 5: Probability of finding an electron in the upper $N_\uparrow$ or lower $N_\downarrow$ channel for an electron originally injected into the lower channel. The simulations using the fine grid have similar results, with the CN results obscuring the view of explicit ones, and differ considerably from those of the coarse grid.

	static barrier	variable barrier
explicit, coarse	26 s	32 s
explicit, fine	247 s	302 s
ADHIE	35 s	44 s
CN	171 s	3118 s

Table 2: The single-core calculation times for the different methods with either a static or variable barrier. The calculation times for the static barrier are averaged over 15 simulations, each with a different barrier height.

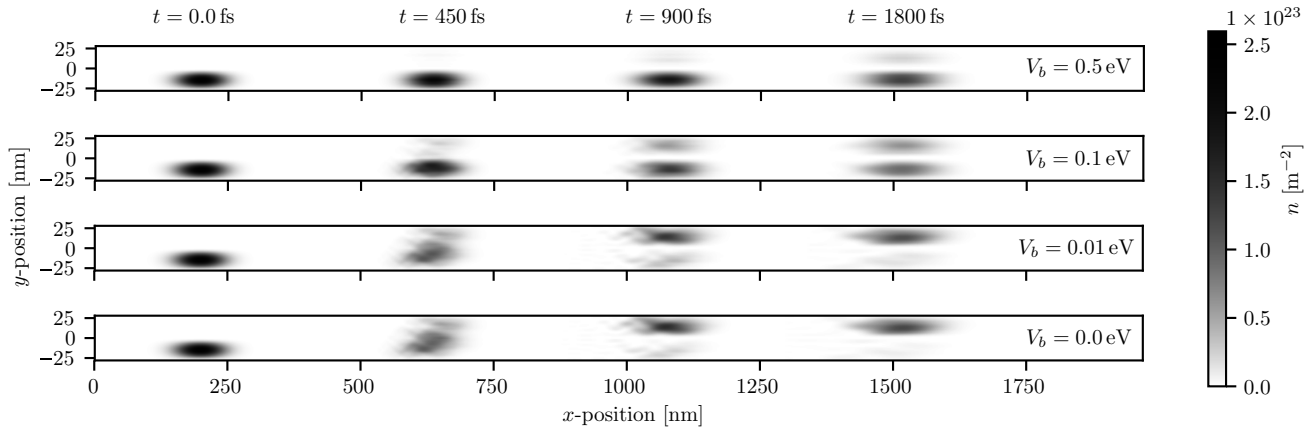

Figure 6: A flying qubit traveling through laterally tunnel-coupled quantum wires for different values of the barrier height V_b in the central region between 500 nm and 750 nm. The probability density $n = |\psi|^2$ of the wave packet is shown every 450 fs.

methods are given in Table 2. It is clear that the time step hindering the explicit calculation can be efficiently removed for this set-up as the ADHIE calculation is 7 times faster than the explicit calculation and almost 5 times faster compared to the CN method. This is because the ADHIE method aims to minimize the number of implicit calculations and therefore results in a much more efficient scheme. Note that for the ADHIE and CN schemes, the implicit calculations were performed by first calculating the LU decomposition prior to the FDTD loop. The computation time needed for the LU decomposition is included in the number shown in Table 2.

In Fig. 6, the probability density $n = |\psi|^2$ is plotted for different values of the barrier height V_b as the particle propagates from the lower left to the right calculated with the ADHIE method. It can be seen that the wave packet spreads out over time in the direction of propagation and tunnels from the lower to the upper channel depending on the barrier height V_b.

The second set of calculations considers a time-dependent barrier height in the central region. The scattering region again starts 500 nm from the left side but now has length $w = 1000\,\mathrm{nm}$. The barrier height is modulated in time as

$$V_b(t) = 0.25\,\mathrm{eV}(1 + \cos(\omega t)), \tag{80}$$

with $\omega = 20.0\,\mathrm{Trad\,s^{-1}}$. Hence, at $t = 0$ the barrier in the central region is the same as the barrier height separating the 2 channels.

In Fig. 7, the probability current I

$$I = \int_{S_{\uparrow(\downarrow)}} \boldsymbol{j} \cdot \boldsymbol{n}\,\mathrm{d}S \tag{81}$$

through the upper and lower channel at position $x = 1700\,\mathrm{nm}$ is plotted as a function of time for the various methods. Again, the coarse grid is unable to correctly predict the behavior of the wave packet. While the other three methods yield similar results, the CN method has the largest deviation from the other two. Even though the method is stable for every time step, $\Delta t_{\mathrm{CN}} = 700\,\mathrm{fs}$ is slightly too large to obtain accurate calculations. These results are confirmed in Fig. 8 where the probability density $n = |\psi|^2$ is plotted for the various calculation methods every 450 fs.

For a time-dependent potential, it is still possible to compute the LU-factorization of the matrices prior to the FDTD loop if the ADHIE scheme is used. However, this is not possible for the CN scheme as the potential enters the matrix that has to be inverted. Hence, the linear system of equations has to be

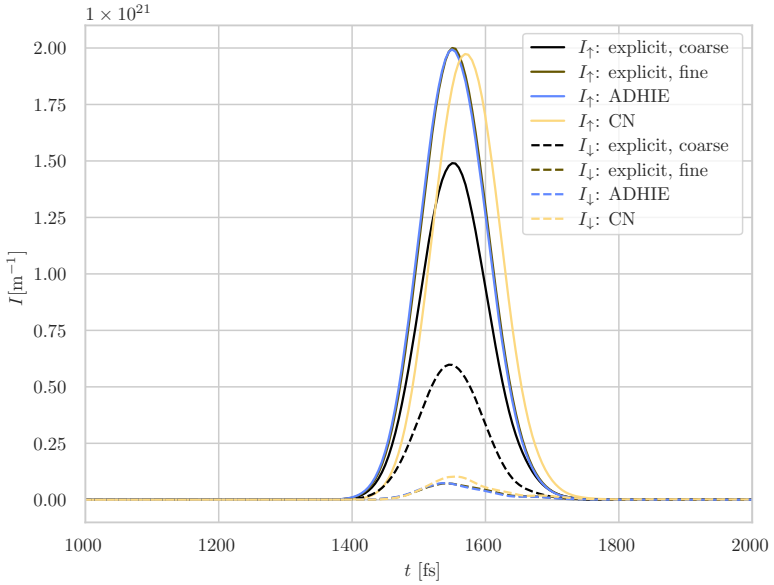

Figure 7: The probability current as a function of time through the plane $x = 1700\,\text{nm}$ in the upper and lower channels calculated with the various methods. The solid and dashed lines show the current in the upper and lower channel, respectively. The curves for the explicit fine simulations are almost completely covered by the curves for the ADHIE method.

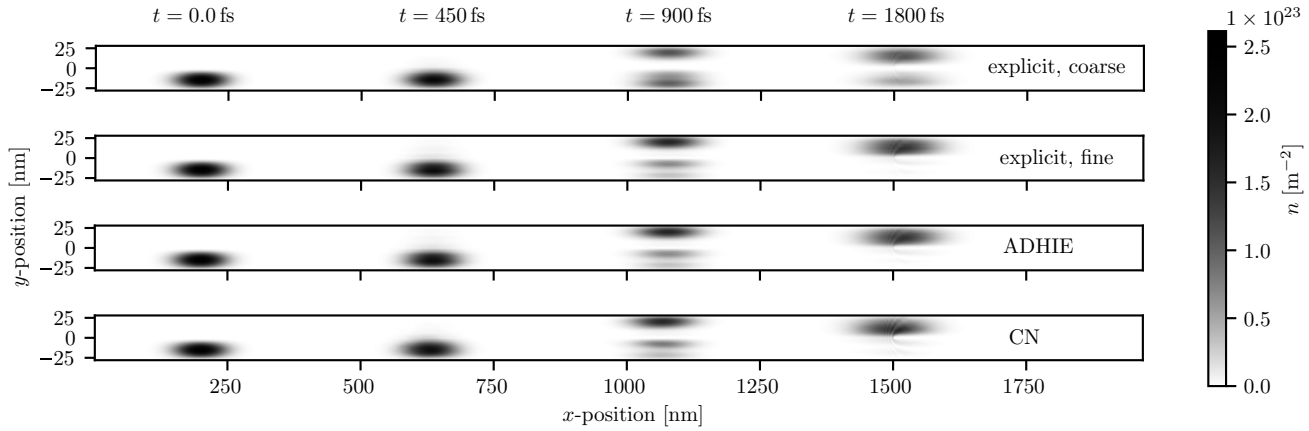

Figure 8: A flying qubit traveling through laterally tunnel-coupled quantum wires for different simulation methods. The probability density $n = |\psi|^2$ of the wave packet is shown every 450 fs. A time-varying barrier height is used according to (80) between 500 nm and 1500 nm. The first simulation uses the coarse uniform grid while the others use the nonuniform grid described above. The coarse grid yields a different result compared to the other simulations. The CN method yields approximately the same behavior for the wave packet, but it lags somewhat behind.

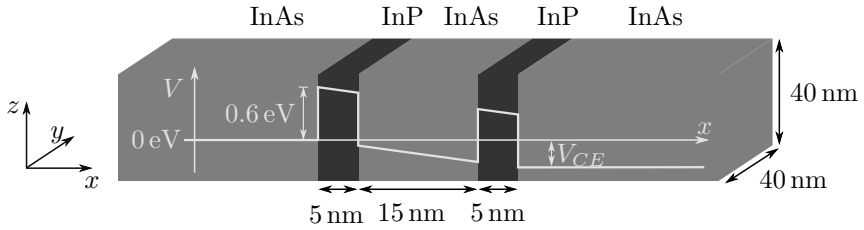

Figure 9: Schematic of a square nanowire double-barrier resonant-tunneling diode. The nanowire is assumed infinite in the x-direction. A voltage V_{CE} is applied, resulting in a linear decrease of the potential energy surface over the double-barrier structure. The effective mass of an electron in InAs and InP are $m_{\mathrm{InAs}} = 0.023\, m_{\mathrm{e}}$ and $m_{\mathrm{InP}} = 0.077\, m_{\mathrm{e}}$, respectively.

solved from scratch at every time step and this drastically increases the computation time. The resulting calculation times for the four simulations are also shown in Table 2. The ratios of the computation times stay approximately the same for all simulations except for CN. The latter is approximately 70 times slower than the ADHIE method, as ADHIE can still utilize predetermined LU factors. Moreover, the explicit method now easily outperforms the CN method, but it is still considerably slower than the ADHIE method.

4.5. Nanowire resonant-tunneling diode

In this section, the transmission probability through a nanowire double-barrier resonant-tunneling diode is calculated. The structure discussed here is similar to the one discussed in [1, 2] and constructed in [72]. The resonant-tunneling diode is defined by two InP barriers of height $V = 0.6\,\mathrm{eV}$ in an InAs nanowire. The nanowire has a square cross-section with sides 40 nm and it has a longitudinal potential profile as shown in Fig. 9, where V_{CE} is the applied voltage. The effective masses in InAs and InP are $m_{\mathrm{InAs}} = 0.023\, m_{\mathrm{e}}$ and $m_{\mathrm{InP}} = 0.077\, m_{\mathrm{e}}$, respectively. The extension of the presented ADHIE method to include a variable mass is presented in Appendix B. A wave packet is inserted in the nanowire using a total-field scattered-field (TFSF) boundary [11]. As such, the computational domain can be smaller than the wave packet, expediting the computation. A Gaussian wave packet is inserted with central energy $E = 0.08\,\mathrm{eV}$ and width $\sigma = 10\,\mathrm{nm}$. The wave packet is in the transversal ground state.

The transmission probability, as a function of the injected energy at a particular bias voltage V_{CE}, is calculated by averaging the outgoing wave function over the transversal direction, taking the Fourier transform of this signal and dividing it by the analytical signal when no barrier or bias is present

$$T(E, V_{CE}) = \left| \frac{\Psi_{\mathrm{calc}}(E, V_{CE})}{\Psi_{\mathrm{analytic}}(E)} \right|^2 . \tag{82}$$

The current is calculated as in [73] with

$$I(V_{CE}) = \frac{2e}{\pi\hbar}\sqrt{E_0} \int_{E_0}^{\infty} T(E, V_{CE})(E - E_0)^{-1/2} \left(\frac{1}{1 + \exp\left(\frac{E - E_F}{kT}\right)} - \frac{1}{1 + \exp\left(\frac{E - E_F - eV_{CE}}{kT}\right)} \right) \mathrm{d}E\,, \tag{83}$$

where $E_0 = 20.436\,\mathrm{meV}$ is the transversal ground state energy.

The transmission is calculated by performing a time-dependent simulation and using (82) for every applied voltage V_{CE}. The Fermi level E_F was determined to be 2 meV above the first subband minimum, such that $E_F = 22.436\,\mathrm{meV}$ [2]. Several discretizations are used in the x-direction. The first discretization D_1 is from $-200\,\mathrm{nm}$ to $200\,\mathrm{nm}$ with uniform cells of width $\Delta x = 2.5\,\mathrm{nm}$, resulting in 160 cells in the x-direction. Next, D_1 is uniformly refined several times. The resulting discretizations are D_2 with 400 cells and $\Delta x = 1\,\mathrm{nm}$, D_3 with 800 cells and $\Delta x = 0.5\,\mathrm{nm}$, and D_4 with 1600 cells and $\Delta x = 0.25\,\mathrm{nm}$. The last discretization D_5 is a nonuniform discretization, as follows: from $-200.0\,\mathrm{nm}$ to $-30.0\,\mathrm{nm}$ and from 30.0 nm to 200.0 nm, the grid has uniform cells of width $\Delta x = 2\,\mathrm{nm}$. Between $-12.5\,\mathrm{nm}$ and 12.5 nm, D_5 has cells

Simulation	S_1	S_2	S_3	S_4	S_5	S_6
Discretization	D_1	D_2	D_3	D_4	D_5	D_5
Method	explicit	explicit	explicit	explicit	explicit	ADHIE
Δt	301.0 as	132.4 as	44.14 as	12.04 as	12.04 as	256.5 as
CPU time	57 s	296 s	1839 s	14 701 s	2364 s	167 s

Table 3: The different simulations parameters corresponding to S_1 to S_6. The discretization, calculation method, time step and resulting average single-core CPU times per applied voltage are given. The time step was calculated with (36) using the infinity norm instead of the 2-norm.

of width $\Delta x = 0.25\,\text{nm}$, just like D_4. In the intermediate areas, the cell sizes are graded with a constant grading ratio resulting in a total of 312 cells. For all discretizations, the y- and z-directions are uniformly meshed with 20 cells of width 2 nm. The wave function is inserted using a TFSF boundary at $x = -40\,\text{nm}$ with an initial pulse center at $x = -240.0\,\text{nm}$. As such, there is no particle in the active domain at initialization. On both sides, there is a 150 nm thick PML.

Several sets of simulations are performed. Sets S_1, S_2, S_3 and S_4 use discretizations D_1, D_2, D_3 and D_4, respectively. Sets S_1 to S_4 solve the problem fully explicitly and, hence, represent a standard uniform refinement strategy. It is expected that the simulations converge to the exact result. Sets S_5 and S_6 both use discretization D_5 and represent a more advanced nonuniform refinement strategy. While S_5 solves the complete problem explicitly, S_6 solves the area between $x = -30.0\,\text{nm}$ and $x = 30.0\,\text{nm}$ implicitly in the x-direction but explicitly in the other two sections along the x-direction (from $-200.0\,\text{nm}$ till $-30.0\,\text{nm}$ and from 30.0 nm till 200.0 nm) and also along the y- and z-directions, this by using the ADHIE method. Each simulation terminates after a physical simulation time of 10.0 ps. However, because transmission through the double barriers is a resonant process, the decay time is very long. As such, the signal is extrapolated using the matrix-pencil method [74] until it has mostly decayed. The various simulation parameters are summarized in Table 3 with the average single-core CPU time per applied voltage.

In Fig. 10a, the transmission coefficients $T(E, V_{CE})$ calculated by (82) at applied voltages $V_{CE} = 0.0\,\text{mV}$ and $V_{CE} = 73.0\,\text{mV}$ are shown. The resulting IV-characteristic of the device using (83) is shown in Fig. 10b. The IV-curve for S_1 misjudges the amplitude of the peak current by over an order of magnitude. The curves for S_2 and S_3 seem to converge to the value obtained for S_4. The results for S_5 and S_6 are in very close agreement with S_4 such that they are difficult to distinguish. Moreover, the peak voltage of $V_{CE} = 72\,\text{mV}$ obtained for S_4 to S_6 is close to the value of 72.4 mV for a cylindrical wire, obtained from a 1-D transfer matrix calculation in both [2] and [73]. The computation times listed in Table 3 show that uniform refinement greatly increases the computation time. Simulation S_4 takes, for example, more than 250 times longer than S_1. Using a nonuniform grid can decrease the computation time considerably as S_5 is already 6 times faster than S_4 at no cost to the accuracy. The small time step hindering S_5 can be increased by using the ADHIE method. As such, S_6 is 14 times faster than S_5, making it almost 90 times faster than S_4. Hence, it is clear that the ADHIE method outperforms the explicit method for balancing accuracy with efficiency in cases where the grid is very nonuniform.

5. Conclusion

In this paper, a method was proposed for solving the time-dependent Schrödinger equation on nonuniform tensor-product grids. The method combines an implicit scheme with an explicit one to increase the overall time step imposed by the explicit scheme on finely meshed regions of the grid. A rigorous stability analysis has shown that it is possible to easily and efficiently remove small cells from the stability criterion. By treating the different directions separately and only solving part of the grid implicitly, the performed simulations show that this yields a much reduced computational cost compared to fully implicit methods.

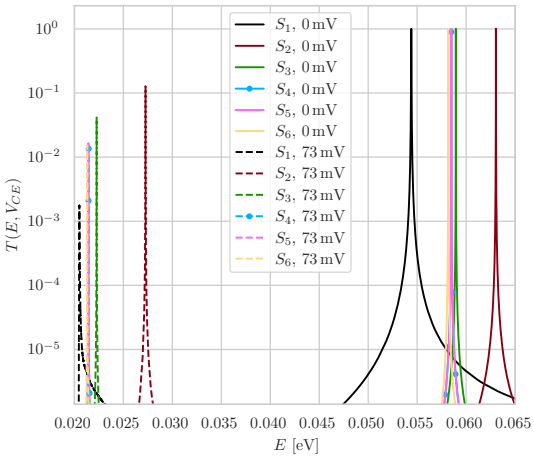

(a) The transmission coefficients at applied voltages $V_{CE} = 0.0\,\text{mV}$ and $V_{CE} = 73.0\,\text{mV}$ obtained with (82).

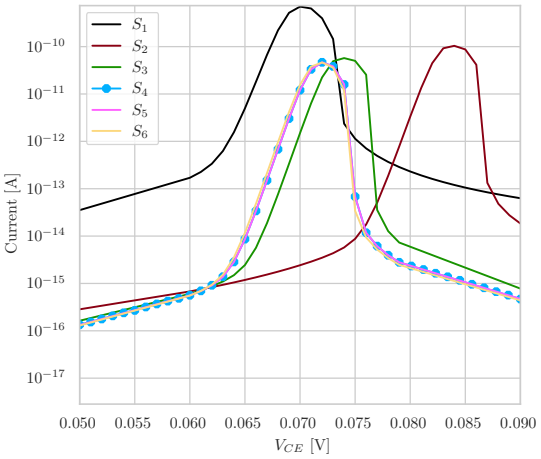

(b) The IV-characteristic obtained with (83)

Figure 10: The transmission coefficients $T(E, V_{CE})$ and the resulting IV-characteristics.

Moreover, the method scales linearly with the problem size, making it highly applicable for large computational domains in 2-D and 3-D. Noteworthy is that the potential energy is not included in the implicit part of the calculation. As such, a time-varying potential can be easily added without changing the implicit part of the calculation. This is unlike other implicit methods, such as the Crank-Nicolson method, where a linear system of equations has to be solved from scratch at every time step. The inclusion of a time-dependent potential is important for simulating transient behavior in nanodevices or when including the Coulomb interaction between different particles.
Future studies aim to extend this method to higher-order accurate methods. However, providing a rigorous mathematical proof for such schemes is very challenging. Equally interesting is to investigate if other hybrid methods can be developed in the same spirit based on other implicit or explicit schemes.

Appendix A. Second-order partial derivative on a nonuniform grid

In this section we will derive our approximation to the second-order partial derivative and discuss the truncation error in 2-D.
Consider the function f which is discretized on a 2-D nonuniform grid. The Taylor expansion of $f|_{i+1,j}$ and $f|_{i-1,j}$ around the coordinate (x_i, y_j) is given by:

$$f|_{i+1,j} = f|_{i,j} + \Delta x_{i+1} \left.\frac{\partial f}{\partial x}\right|_{i,j} + \frac{{\Delta x_{i+1}}^2}{2} \left.\frac{\partial^2 f}{\partial x^2}\right|_{i,j} + \frac{{\Delta x_{i+1}}^3}{6} \left.\frac{\partial^3 f}{\partial x^3}\right|_{i,j} + \mathcal{O}\big({\Delta x_{i+1}}^4\big), \tag{A.1}$$

$$f|_{i-1,j} = f|_{i,j} - \Delta x_i \left.\frac{\partial f}{\partial x}\right|_{i,j} + \frac{{\Delta x_i}^2}{2} \left.\frac{\partial^2 f}{\partial x^2}\right|_{i,j} - \frac{{\Delta x_i}^3}{6} \left.\frac{\partial^3 f}{\partial x^3}\right|_{i,j} + \mathcal{O}\big({\Delta x_i}^4\big). \tag{A.2}$$

Dividing (A.1) by $\Delta x_i^\star \Delta x_{i+1}$ and (A.2) by $\Delta x_i^\star \Delta x_i$ and adding the results, yields:

$$\begin{aligned} &\frac{f|_{i+1,j} - f|_{i,j}}{\Delta x_{i+1}\Delta x_i^\star} - \frac{f|_{i,j} - f|_{i-1,j}}{\Delta x_i^\star \Delta x_i} \\ &\quad = \frac{(\Delta x_{i+1} + \Delta x_i)/2}{\Delta x_i^\star} \left.\frac{\partial^2 f}{\partial x^2}\right|_{i,j} + \frac{\left({\Delta x_{i+1}}^2 - {\Delta x_i}^2\right)}{6\Delta x_i^\star} \left.\frac{\partial^3 f}{\partial x^3}\right|_{i,j} + \mathcal{O}\left(\frac{{\Delta x_i}^3 + {\Delta x_{i+1}}^3}{\Delta x_i^\star}\right). \end{aligned} \tag{A.3}$$

This can be simplified by using $\Delta x_i^\star = (\Delta x_i + \Delta x_{i+1})/2$ as:

$$\left.\frac{\partial^2 f}{\partial x^2}\right|_{i,j} = \frac{f|_{i+1,j} - f|_{i,j}}{\Delta x_{i+1}\Delta x_i^\star} - \frac{f|_{i,j} - f|_{i-1,j}}{\Delta x_i^\star \Delta x_i} + \frac{\Delta x_{i+1} - \Delta x_i}{3} \left.\frac{\partial^3 f}{\partial x^3}\right|_{i,j} + \mathcal{O}\big({\Delta x_{i+1}}^2 - \Delta x_{i+1}\Delta x_i + {\Delta x_i}^2\big). \tag{A.4}$$

An analogous result can be obtained for the second-order partial derivative in the y-direction. Equation (A.4) implies that the truncation error for a second-order partial derivative – and thus also the spatially discretized Hamiltonian (7) – is proportional to the difference in cell size of two subsequent cells along the direction of the derivative. For smoothly varying grids, this results in a highly-accurate scheme which becomes second-order accurate in the limit of uniform grids.

Appendix B. Variable mass ADHIE

The Schrödinger equation for a variable mass is given by

$$\jmath\hbar\frac{\partial}{\partial t}\psi = -\frac{\hbar^2}{2}\boldsymbol{\nabla}\cdot\left(\frac{1}{m}\boldsymbol{\nabla}\psi\right) + V\psi. \tag{B.1}$$

For simplicity, we only consider a mass which is variable in a single direction, here the x-direction. Also only implicitization along x is considered. The resulting spatial discretization yields

$$\jmath\hbar\frac{\partial}{\partial t}\boldsymbol{\psi} = (T_x + T_y + T_z + V)\boldsymbol{\psi}, \tag{B.2}$$

with

$$T_x = \frac{\hbar^2}{2}\left(\delta_x^{\star\,-1} D_x^T m^{\star\,-1} {\delta_x}^{-1} D_x\right) \otimes I_{n_y-1} \otimes I_{n_z-1}, \tag{B.3}$$

$$T_y = \frac{\hbar^2}{2} m^{-1} \otimes \left(\delta_y^{\star\,-1} D_y^T {\delta_y}^{-1} D_y\right) \otimes I_{n_z-1}, \tag{B.4}$$

$$T_z = \frac{\hbar^2}{2} m^{-1} \otimes I_{n_y-1} \otimes \left(\delta_z^{\star\,-1} D_z^T {\delta_z}^{-1} D_z\right), \tag{B.5}$$

with m the diagonal matrix containing the variable mass in the x-direction on the vertices of the primary grid, excluding the edge of the grid, and $m^\star$ containing the mass harmonically averaged from the masses on the primary grid.
The resulting ADHIE scheme is given by

$$\begin{bmatrix} G & -\Delta\nu H \\ 0 & G \end{bmatrix} \boldsymbol{x}|^{n+1} = \begin{bmatrix} G & 0 \\ -\Delta\nu H & G \end{bmatrix} \boldsymbol{x}|^{n}, \tag{B.6}$$

where

$$H = T_x + T_y + T_z, \tag{B.7}$$

$$G = \left(I_{n_x-1} + \frac{\Delta\nu}{2} S_x\right) \otimes I_{n_y-1} \otimes I_{n_z-1}, \tag{B.8}$$

and

$$S_x = \frac{\hbar^2}{2}\left(\delta_x^{\star\,-1} D_x^T m^{\star\,-1} P_x {\delta_x}^{-1} D_x\right) \tag{B.9}$$

The same method to prove the stability as in Section 3 is used. First, the equations are symmetrized using Q, defined in (25), resulting in

$$\begin{bmatrix} \tilde{G} & -\Delta\nu \tilde{H} \\ 0 & \tilde{G} \end{bmatrix} \tilde{\boldsymbol{x}}|^{n+1} = \begin{bmatrix} \tilde{G} & 0 \\ -\Delta\nu \tilde{H} & \tilde{G} \end{bmatrix} \tilde{\boldsymbol{x}}|^{n}, \tag{B.10}$$

with

$$\tilde{H} = \tilde{T}_x + \tilde{T}_y + \tilde{T}_z, \tag{B.11}$$

$$\tilde{G} = \left(I_{n_x-1} + \frac{\Delta\nu}{2}\tilde{S}_x \right) \otimes I_{n_y-1} \otimes I_{n_z-1}, \tag{B.12}$$

$$\tilde{T}_x = \frac{\hbar^2}{2}\left({\delta_x^\star}^{-1/2} D_x^T {m^\star}^{-1} {\delta_x}^{-1} D_x {\delta_x^\star}^{-1/2} \right) \otimes I_{n_y-1} \otimes I_{n_z-1}, \tag{B.13}$$

$$\tilde{T}_y = \frac{\hbar^2}{2} m^{-1} \otimes \left({\delta_y^\star}^{-1/2} D_y^T {\delta_y}^{-1} D_y {\delta_y^\star}^{-1/2} \right) \otimes I_{n_z-1}, \tag{B.14}$$

$$T_z = \frac{\hbar^2}{2} m^{-1} \otimes I_{n_y-1} \otimes \left({\delta_z^\star}^{-1/2} D_z^T {\delta_z}^{-1} D_z {\delta_z^\star}^{-1/2} \right) \tag{B.15}$$

and

$$\tilde{S}_x = \frac{\hbar^2}{2}\left({\delta_x^\star}^{-1/2} D_x^T {m^\star}^{-1} P_x {\delta_x}^{-1} D_x {\delta_x^\star}^{-1/2} \right). \tag{B.16}$$

The matrices with a tilde are all symmetric. The symmetrized update scheme (B.10) can be rewritten in exactly the same way as (33)–(35). Again, stability is guaranteed when E in (34) is positive definite. For the system (B.10), E is rewritten as

$$E = \begin{bmatrix} I_n & -\frac{\Delta\nu}{2}\left(\tilde{U}_x + \tilde{T}_y + \tilde{T}_z + V \right) \\ -\frac{\Delta\nu}{2}\left(\tilde{U}_x + \tilde{T}_y + \tilde{T}_z + V \right) & I_n \end{bmatrix} + \left(\frac{\Delta\nu}{2} \right) \begin{bmatrix} \tilde{S}_x & -\tilde{S}_x \\ -\tilde{S}_x & \tilde{S}_x \end{bmatrix} \otimes I_{n_y-1} \otimes I_{n_z-1}. \tag{B.17}$$

with

$$U_x = \tilde{T}_x - \tilde{S}_x \otimes I_{n_y-1} \otimes I_{n_z-1} \tag{B.18}$$

$$= \left({\delta_x^\star}^{-1/2} D_x^T {m^\star}^{-1} {\delta_x}^{-1} (I_{n_x} - P_x) D_x {\delta_x^\star}^{-1/2} \right) \otimes I_{n_y-1} \otimes I_{n_z-1}. \tag{B.19}$$

Matrix $\tilde{S}_x$ can be proven to be positive semi-definite in the same way as (50). This immediately shows, by virtue of (47)–(49), that the second term in (B.17) is positive semi-definite as well. It is now easy to prove that the first term in (B.17) is positive definite for

$$\Delta t < \frac{2\hbar}{\left\| \tilde{U}_x + \tilde{T}_y + \tilde{T}_z + V \right\|_2}. \tag{B.20}$$

As such, the update scheme is stable for a time step satisfying (B.20).

References

[1] M. Zervos and L. F. Feiner, "Electronic structure of piezoelectric double-barrier InAs/InP/InAs/InP/InAs (111) nanowires," *J. Appl. Phys.*, vol. 95, no. 1, pp. 281–291, 2004.

[2] M. Zervos and N. T. Pelekanos, "Current transport in semiconductor nanowires with built-in barriers based on a 1D transfer matrix calculation," *J. Appl. Phys.*, vol. 104, no. 5, 2008.

[3] L. Pierantoni, D. Mencarelli, and T. Rozzi, "A New 3-D Transmission Line Matrix Scheme for the Combined Schrödinger–Maxwell Problem in the Electronic/Electromagnetic Characterization of Nanodevices," *IEEE Trans. Microw. Theory Tech.*, vol. 56, pp. 654–662, mar 2008.

[4] L. Pierantoni, D. Mencarelli, and T. Rozzi, "Boundary immittance operators for the Schrödinger-Maxwell problem of carrier dynamics in nanodevices," *IEEE Trans. Microw. Theory Tech.*, vol. 57, no. 5, pp. 1147–1155, 2009.

[5] J. F. Mennemann, A. Jüngel, and H. Kosina, "Transient Schrödinger-Poisson simulations of a high-frequency resonant tunneling diode oscillator," *J. Comput. Phys.*, vol. 239, pp. 187–205, 2013.

[6] M. Zervos, "Electronic properties of core-shell nanowire resonant tunneling diodes," *Nanoscale Res. Lett.*, vol. 9, no. 1, pp. 1–8, 2014.

[7] D. M. Sullivan, S. Mossman, and M. G. Kuzyk, "Time-Domain Simulation of Three Dimensional Quantum Wires," *PLoS One*, vol. 11, Apr. 2016.

[8] J. A. Del Alamo and C. C. Eugster, "Quantum field-effect directional coupler," *Appl. Phys. Lett.*, vol. 56, no. 1, pp. 78–80, 1990.
[9] H. Gotoh, M. Koshiba, and R. Kaji, "Finite element solution of electron waveguide discontinuities and its application to quantum field effect directional couplers," *IEEE J. Quantum Electron.*, vol. 32, no. 10, pp. 1826–1832, 1996.
[10] D. Mencarelli, T. Rozzi, and L. Pierantoni, "Scattering matrix approach to multichannel transport in many lead graphene nanoribbons," *Nanotechnology*, vol. 21, no. 15, 2010.
[11] J. F. Mennemann and A. Jüngel, "Perfectly Matched Layers versus discrete transparent boundary conditions in quantum device simulations," *J. Comput. Phys.*, vol. 275, pp. 1–24, 2014.
[12] S. Kim, A. Konar, W. S. Hwang, J. H. Lee, J. Lee, J. Yang, C. Jung, H. Kim, J. B. Yoo, J. Y. Choi, Y. W. Jin, S. Y. Lee, D. Jena, W. Choi, and K. Kim, "High-mobility and low-power thin-film transistors based on multilayer MoS2 crystals," *Nat. Commun.*, vol. 3, 2012.
[13] K. Tomioka, M. Yoshimura, and T. Fukui, "A III-V nanowire channel on silicon for high-performance vertical transistors," *Nature*, vol. 488, no. 7410, pp. 189–192, 2012.
[14] D. Sarkar, W. Liu, X. Xie, A. C. Anselmo, S. Mitragotri, and K. Banerjee, "MoS2 field-effect transistor for next-generation label-free biosensors," *ACS Nano*, vol. 8, no. 4, pp. 3992–4003, 2014.
[15] J. Kang, Y. Matsumoto, X. Li, J. Jiang, X. Xie, K. Kawamoto, M. Kenmoku, J. H. Chu, W. Liu, J. Mao, K. Ueno, and K. Banerjee, "On-chip intercalated-graphene inductors for next-generation radio frequency electronics," *Nat. Electron.*, vol. 1, pp. 46–51, 2018.
[16] N. Sai, N. Bushong, R. Hatcher, and M. Di Ventra, "Microscopic current dynamics in nanoscale junctions," *Phys. Rev. B - Condens. Matter Mater. Phys.*, vol. 75, no. 11, pp. 1–8, 2007.
[17] M. Di Ventra, *Electrical Transport in Nanoscale Systems*. Cambridge University Press, 2008.
[18] M. Claus, S. Blawid, S. Mothes, and M. Schroter, "High-Frequency Ballistic Transport Phenomena in Schottky Barrier CNTFETs," *IEEE Trans. Electron Devices*, vol. 59, pp. 2610–2618, Oct. 2012.
[19] S. Andermatt, M. H. Bani-Hashemian, F. Ducry, S. Brück, S. Clima, G. Pourtois, J. Vandevondele, and M. Luisier, "Microcanonical RT-TDDFT simulations of realistically extended devices," *J. Chem. Phys.*, vol. 149, no. 12, 2018.
[20] F. I. Moxley, D. T. Chuss, and W. Dai, "A generalized finite-difference time-domain scheme for solving nonlinear Schrödinger equations," *Comput. Phys. Commun.*, vol. 184, no. 8, pp. 1834–1841, 2013.
[21] B. Reichel and S. Leble, "On convergence and stability of a numerical scheme of Coupled Nonlinear Schrödinger Equations," *Comput. Math. with Appl.*, vol. 55, no. 4, pp. 745–759, 2008.
[22] Y. Xu and L. Zhang, "Alternating direction implicit method for solving two-dimensional cubic nonlinear Schrödinger equation," *Comput. Phys. Commun.*, vol. 183, no. 5, pp. 1082–1093, 2012.
[23] C. Zheng, "A perfectly matched layer approach to the nonlinear Schrödinger wave equations," *J. Comput. Phys.*, vol. 227, no. 1, pp. 537–556, 2007.
[24] R. Eskar, P. Huang, and X. Feng, "A new high-order compact ADI finite difference scheme for solving 3D nonlinear Schrödinger equation," *Adv. Differ. Equations*, vol. 2018, p. 286, Dec. 2018.
[25] J. P. Wilson, "Generalized Finite-Difference Time-Domain method with absorbing boundary conditions for solving the nonlinear Schrödinger equation on a GPU," *Comput. Phys. Commun.*, vol. 235, pp. 279–292, 2019.
[26] Q. Chang, E. Jia, and W. Sun, "Difference Schemes for Solving the Generalized Nonlinear Schrödinger Equation," *J. Comput. Phys.*, vol. 148, no. 2, pp. 397–415, 1999.
[27] F. I. Moxley, T. Byrnes, B. Ma, Y. Yan, and W. Dai, "A G-FDTD scheme for solving multi-dimensional open dissipative Gross-Pitaevskii equations," *J. Comput. Phys.*, vol. 282, pp. 303–316, 2015.
[28] I. W. Sudiarta and D. J. W. Geldart, "Solving the Schrödinger equation using the finite difference time domain method," *J. Phys. A Math. Theor.*, vol. 40, pp. 1885–1896, Feb. 2007.
[29] M. Strickland and D. Yager-Elorriaga, "A parallel algorithm for solving the 3d Schrödinger equation," *J. Comput. Phys.*, vol. 229, no. 17, pp. 6015–6026, 2010.
[30] I. W. Sudiarta and L. M. Angraini, "The finite difference time domain (FDTD) method to determine energies and wave functions of two-electron quantum dot," *AIP Conf. Proc.*, 2018.
[31] L. M. Angraini and I. W. Sudiarta, "Non-Standard and Numerov Finite Difference Schemes for Finite Difference Time Domain Method to Solve One-Dimensional Schrödinger Equation," *J. Phys. Theor. Appl.*, vol. 2, no. 1, p. 27, 2018.
[32] J. Crank and P. Nicolson, "A practical method for numerical evaluation of solutions of partial differential equations of the heat-conduction type," *Math. Proc. Cambridge Philos. Soc.*, vol. 43, no. 1, pp. 50–67, 1947.
[33] A. Goldberg, H. M. Schey, and J. L. Schwartz, "Computer-Generated Motion Pictures of One-Dimensional Quantum-Mechanical Transmission and Reflection Phenomena," *Am. J. Phys.*, vol. 35, pp. 177–186, Mar. 1967.
[34] L. Bian, G. Pang, S. Tang, and A. Arnold, "ALmost EXact boundary conditions for transient Schrödinger-Poisson system," *J. Comput. Phys.*, vol. 313, pp. 233–246, 2016.
[35] J. Douglas Jr., "Alternating direction methods for three space variables," *Numer. Math.*, vol. 4, no. 1, pp. 41–63, 1962.
[36] S. Zhai, X. Feng, and Z. Weng, "New High-Order Compact ADI Algorithms for 3D nonlinear Time-Fractional Convection-Diffusion Equation," *Math. Probl. Eng.*, vol. 2013, 2013.
[37] S. Zhai, X. Feng, and Y. He, "A New High-Order Compact ADI Method for 3-D Unsteady Convection-Diffusion Problems with Discontinuous Coefficients," *Numer. Heat Transf. Part B Fundam.*, vol. 65, no. 4, pp. 376–391, 2014.
[38] M. Dehghan, "Finite difference procedures for solving a problem arising in modeling and design of certain optoelectronic devices," *Math. Comput. Simul.*, vol. 71, no. 1, pp. 16–30, 2006.
[39] W. C. Tay and E. L. Tan, "Pentadiagonal alternating-direction-implicit finite-difference time-domain method for two-dimensional Schrödinger equation," *Comput. Phys. Commun.*, vol. 185, no. 7, pp. 1886–1892, 2014.
[40] A. Askar and A. S. Cakmak, "Explicit integration method for the time-dependent Schrodinger equation for collision

problems," *J. Chem. Phys.*, vol. 68, no. 6, pp. 2794–2798, 1978.
[41] P. Decleer, A. Van Londersele, H. Rogier, and D. Vande Ginste, "Nonuniform and Higher-order FDTD Methods for the Schrödinger Equation," *J. Comput. Appl. Math.*, vol. 381, p. 113023, jan 2021.
[42] P. B. Visscher, "A fast explicit algorithm for the time-dependent Schrödinger equation," *Comput. Phys.*, vol. 5, no. 6, p. 596, 1991.
[43] A. Soriano, E. A. Navarro, J. A. Portí, and V. Such, "Analysis of the finite difference time domain technique to solve the Schrödinger equation for quantum devices," *J. Appl. Phys.*, vol. 95, no. 12, pp. 8011–8018, 2004.
[44] W. Dai, G. Li, R. Nassar, and S. Su, "On the stability of the FDTD method for solving a time-dependent Schrödinger equation," *Numer. Methods Partial Differ. Equ.*, vol. 21, no. 6, pp. 1140–1154, 2005.
[45] D. M. Sullivan and D. S. Citrin, "Determination of the eigenfunctions of arbitrary nanostructures using time domain simulation," *J. Appl. Phys.*, vol. 91, no. 5, pp. 3219–3226, 2002.
[46] D. M. Sullivan and D. S. Citrin, "Determining quantum eigenfunctions in three-dimensional nanoscale structures," *J. Appl. Phys.*, vol. 97, no. 10, pp. 10–16, 2005.
[47] D. M. Sullivan and P. M. Wilson, "Time-domain determination of transmission in quantum nanostructures," *J. Appl. Phys.*, vol. 112, no. 6, 2012.
[48] F. I. Moxley III, F. Zhu, and W. Dai, "A Generalized FDTD Method with Absorbing Boundary Condition for Solving a Time-Dependent Linear Schrodinger Equation," *Am. J. Comput. Math.*, vol. 02, no. 03, pp. 163–172, 2012.
[49] F. I. Moxley, T. Byrnes, F. Fujiwara, and W. Dai, "A generalized finite-difference time-domain quantum method for the N-body interacting Hamiltonian," *Comput. Phys. Commun.*, vol. 183, no. 11, pp. 2434–2440, 2012.
[50] A. Gordon, C. Jirauschek, and F. X. Kärtner, "Numerical solver of the time-dependent Schrödinger equation with Coulomb singularities," *Phys. Rev. A - At. Mol. Opt. Phys.*, vol. 73, no. 4, pp. 1–10, 2006.
[51] N. Bigaouette, E. Ackad, and L. Ramunno, "Nonlinear grid mapping applied to an FDTD-based, multi-center 3D Schrödinger equation solver," *Comput. Phys. Commun.*, vol. 183, no. 1, pp. 38–45, 2012.
[52] J. Chen and J. Wang, "A 3D hybrid implicit-explicit FDTD scheme with weakly conditional stability," *Microw. Opt. Technol. Lett.*, vol. 48, pp. 2291–2294, nov 2006.
[53] Q. Zhang, B. Zhou, and J. Wang, "A novel hybrid implicit-explicit fdtd algorithm with more relaxed stability condition," *IEEE Antennas Wirel. Propag. Lett.*, vol. 12, pp. 1372–1375, 2013.
[54] J. Wang, B. Zhou, L. Shi, C. Gao, and B. Chen, "A novel 3-D HIE-FDTD method with one-step leapfrog scheme," *IEEE Trans. Microw. Theory Tech.*, vol. 62, no. 6, pp. 1275–1283, 2014.
[55] A. Van Londersele, D. De Zutter, and D. Vande Ginste, "A New Hybrid Implicit–Explicit FDTD Method for Local Subgridding in Multiscale 2-D TE Scattering Problems," *IEEE Trans. Antennas Propag.*, vol. 64, pp. 3509–3520, aug 2016.
[56] A. Van Londersele, D. De Zutter, and D. Vande Ginste, "An in-depth stability analysis of nonuniform FDTD combined with novel local implicitization techniques," *J. Comput. Phys.*, vol. 342, pp. 177–193, 2017.
[57] A. Van Londersele, D. De Zutter, and D. Vande Ginste, "Full-Wave Analysis of the Shielding Effectiveness of Thin Graphene Sheets with the 3D Unidirectionally Collocated HIE-FDTD Method," *Int. J. Antennas Propag.*, vol. 2017, pp. 1–8, 2017.
[58] A. Van Londersele, D. De Zutter, and D. Vande Ginste, "A Collocated 3-D HIE-FDTD Scheme With PML," *IEEE Microw. Wirel. Components Lett.*, vol. 27, pp. 609–611, jul 2017.
[59] J. Chen, J. Li, and Q. H. Liu, "Designing Graphene-Based Absorber by Using HIE-FDTD Method," *IEEE Trans. Antennas Propag.*, vol. 65, no. 4, pp. 1896–1902, 2017.
[60] J. Chen, J. Guo, and C. Tian, "Analyzing the Shielding Effectiveness of a Graphene-Coated Shielding Sheet by Using the HIE-FDTD Method," *IEEE Trans. Electromagn. Compat.*, vol. 60, no. 2, pp. 362–367, 2018.
[61] M. Dehghan, "A new ADI technique for two-dimensional parabolic equation with an integral condition," *Comput. Math. with Appl.*, vol. 43, no. 12, pp. 1477–1488, 2002.
[62] S. C. Yang, Z. D. Chen, Y. Yu, and W. Y. Yin, "An unconditionally stable one-step arbitrary-order leapfrog ADI-FDTD method and its numerical properties," *IEEE Trans. Antennas Propag.*, vol. 60, no. 4, pp. 1995–2003, 2012.
[63] E. Süli and D. F. Mayers, *An Introduction to Numerical Analysis*. Cambridge University Press, 2008.
[64] R. S. Varga, *Matrix Iterative Analysis*, vol. 27 of *Springer Series in Computational Mathematics*. Springer, 2000.
[65] D. S. Bernstein, *Matrix Mathematics*. Princeton University Press, 2009.
[66] B. Denecker, L. Knockaert, F. Olyslager, and D. De Zutter, "A new state-space-based algorithm to assess the stability of the finite-difference time-domain method for 3D finite inhomogeneous problems," *AEU - Int. J. Electron. Commun.*, vol. 58, no. 5, pp. 339–348, 2004.
[67] A. Bertoni, P. Bordone, R. Brunetti, C. Jacoboni, and S. Reggiani, "Quantum logic gates based on coherent electron transport in quantum wires," *Phys. Rev. Lett.*, vol. 84, no. 25, pp. 5912–5915, 2000.
[68] B. Gaury, J. Weston, M. Santin, M. Houzet, C. Groth, and X. Waintal, "Numerical simulations of time-resolved quantum electronics," *Phys. Rep.*, vol. 534, no. 1, pp. 1–37, 2014.
[69] J. Weston and X. Waintal, "Towards realistic time-resolved simulations of quantum devices," *J. Comput. Electron.*, vol. 15, no. 4, pp. 1148–1157, 2016.
[70] B. Rossignol, T. Kloss, P. Armagnat, and X. Waintal, "Toward flying qubit spectroscopy," *Phys. Rev. B*, vol. 98, no. 20, pp. 1–9, 2018.
[71] M. Yamamoto, S. Takada, C. Bäuerle, K. Watanabe, A. D. Wieck, and S. Tarucha, "Electrical control of a solid-state flying qubit," *Nat. Nanotechnol.*, vol. 7, no. 4, pp. 247–251, 2012.
[72] M. T. Björk, B. J. Ohlsson, C. Thelander, A. I. Persson, K. Deppert, L. R. Wallenberg, and L. Samuelson, "Nanowire resonant tunneling diodes," *Appl. Phys. Lett.*, no. 23, 2002.

[73] R. Ragi, R. V. da Nobrega, and M. A. Romero, "Modeling of peak voltage and current of nanowire resonant tunneling devices: case study on InAs/InP double-barrier heterostructures," *Int. J. Numer. Model. Electron. Networks, Devices Fields*, vol. 26, no. 5, 2013.

[74] J. Ritter and F. Arndt, "Efficient FDTD/Matrix-pencil method for the full-wave scattering parameter analysis of waveguiding structures," *IEEE Trans. Microw. Theory Tech.*, vol. 44, no. 12 PART 2, pp. 2450–2456, 1996.